Asian Journal of Green Chemistry 10 (2026) 694-717

Asian Journal of Green Chemistry

Original Research Article View Article Online | View Journal

Zn-MnO Nanocomposites Derived from *Cocos nucifera*: A Multi-Analytical Characterisation and Antimicrobial Study

Chandrasekhar Maalegoundla[1], Naveen Pusapati[1,2], Lakshmi Satya Boddu[3], Pavan Kumar Naini[1], Sowmyya T[4,*]

[1]*Department of Sciences and Humanities, Matrusri Engineering College, Saidabad, Hyderabad, Telangana—500 059, India*
[2]*Department of Physics, ISBM University, Nawapara (Kosmi), Gariaband, Chhattisgarh- 493 996, India*
[3]*Vishnu Institute of Pharmaceutical Education & Research, Narsapur, Medak, Telangana-502 313, India*
[4]*Forensic Science Unit, Department of Chemistry, University College of Science, Osmania University, Hyderabad, Telangana-500 007, India*

ARTICLE INFORMATION

Submitted: 2025-10-24
Revised: 2025-12-14
Accepted: 2026-01-22
Published: 2026-01-22
Manuscript ID: AJGC-2510-1852
DOI: 10.48309/ajgc.2026.554745.1852

KEYWORDS

Nano Zn-MnO composite
Cocos nucifera
Zeta potential
Antimicrobial activity

ABSTRACT

Structural and morphological properties of nanocomposites make them suitable for biogenic and bioscience applications, in batteries and sensors. The synthesis of Zn-MnO nanocomposites through a green route helps to mitigate ecological deterioration. In the present study, a nano Zn-MnO composite material was synthesized via a green route using the *Cocos nucifera* shell extract as a reducing and capping agent. The synthesized material was calcined at 450, 550, and 650 ℃, and subsequently characterized through X-ray diffraction (XRD), scanning electron microscopy (SEM), energy dispersive X-Ray analysis (EDAX), ultraviolet visible spectroscopy (UV-Vis), Fourier transform infrared spectroscopy (FTIR), Raman spectroscopy, and Zeta potential. Antimicrobial activity was also evaluated. XRD patterns revealed that as the calcination temperature increased, the peaks became sharper, representing the increased crystallinity and crystalline size: 15, 16 and 19 nm, respectively. Peculiar peaks were observed in the UV-Vis spectra with slight variation at 272, 278, and 288 nm. Optical conductivity was found to be 2.466 x 10^9 S^{-1}. Zeta potential values were determined to be -9, -10, and 16 mV, respectively. The band intensity in Raman spectra increased as the calcination temperature rose, suggesting greater phonon coupling and improved crystallinity. FTIR spectral analysis confirmed that Zn–MnO nanoparticles have interacted with organic substances that contain nitrogen, including proteins or amino acid residues, which are likely products of biological agents used in synthesis. Antimicrobial studies showed a maximum inhibition zone of 22 mm against *S. aureus* and 19 mm against *A. niger*. Minimum inhibitory concentration (MIC) results indicated effective bacterial inhibition at 2.5% and fungal inhibition at 5% concentrations.

Corresponding author, E-mail: dr.sowmyya@osmania.ac.in (S. T).
Tel.: +97019 18384

Graphical Abstract

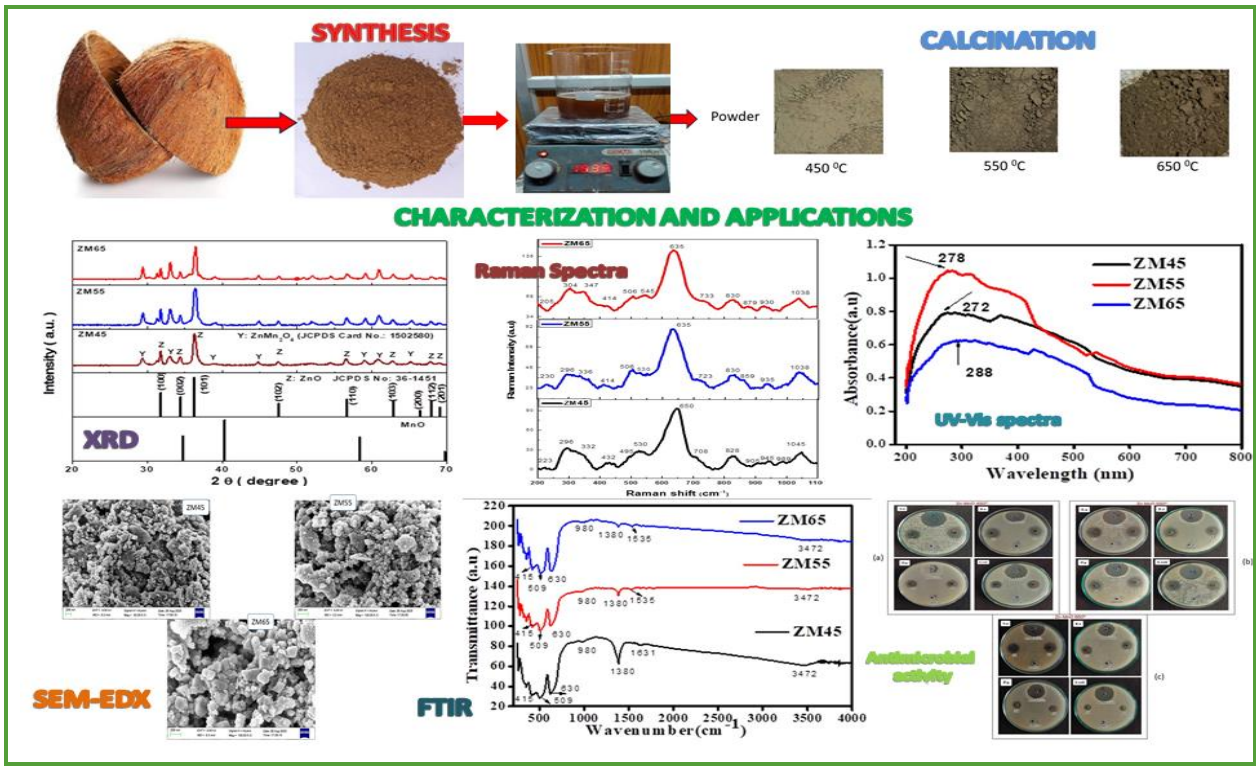

Introduction

The most concerning issue confronting humanity today is environmental pollution, which is also one of the primary ecological causes of disease and mortality. Pollution-related illness was estimated to have contributed to 9 million early deaths in 2015, more than three times the fatalities from AIDS, TB, and malaria. Deforestation, bush burning, the disposal of domestic and agricultural waste in water bodies, the use of pesticides to harvest aquatic life, and the inappropriate disposal of technological trash, all contribute to the pollution of the air, land, and water [1]. The elimination of these contaminants via effective and environmentally friendly techniques is essential. Nanoparticles play vital roles in different areas. Due to their sophisticated optical characteristics, metal oxide nanoparticles may be used in a wide range of scientific disciplines. Metal oxide-based nanomaterials consist of manganese oxides, nanosized iron oxides, titanium oxides, cerium oxides, zinc oxides, magnesium oxides, aluminum oxides, and zirconium oxides [2]. Metal oxide nanoparticles (MO NPs) such as ZnO, TiO_2, Fe_2O_3, and MnO_2, as well as their composites, provide environment friendly and effective solutions for environmental remediation. These nanoparticles help degrade organic contaminants, remove heavy metals, and reduce dangerous compounds in the air, water, and soil. Combining metal oxides such as TiO_2, ZnO, and Fe_2O_3 with carbon-based materials like graphene and activated carbon improves adsorption and catalytic performance for removing airborne pollutants and greenhouse gases like CO, NO_x, and SO_2. When exposed to ultraviolet (UV) or visible light, metal oxides such as ZnO and TiO_2 function as photocatalysts, breaking down organic pollutants in

wastewater. From polluted water, metal oxide nanoparticles, including Fe_2O_3, MnO_2, and ZnO, effectively absorb heavy metals like Pb^{2+}, Hg^{2+}, and As^{3+}. During Fenton or photo-Fenton processes, iron-based nanoparticles (Fe_2O_3 and Fe_3O_4) produce hydroxyl radicals (*OH) that break down organic contaminants. ZnO, MnO_2, and Fe_2O_3 are metal oxides that catalyse the reduction of harmful substances such as dyes, nitrobenzene, and Cr (VI) [3]. Every nanoparticle has its diverse properties, but ZnO, MnO, and their composite nanoparticles are of interest to researchers due to their versatile properties and potential applications**.** Zinc oxide (ZnO) nanoparticles belong to a versatile family of nanomaterials. A wide direct bandgap (3.37 eV), a high exciton binding energy (60 meV), fast electron mobility, high thermal conductivity, and outstanding transparency are all characteristics of zinc oxide (ZnO) [4]. It grows rapidly in various forms and has a wide range of applications in biomedical engineering, environmental remediation, optoelectronics, piezoelectric sensors, UV protection in cosmetics, food preservation, and catalysis [5]. Manganese oxide nanoparticles (MnO_x NPs) semiconducting nature and exist in +2, +3, and +4 oxidation states, making them extremely adaptable for various applications due to their exceptional physicochemical characteristics. Nanoparticles of manganese oxide (MnO) have a wide variety of potential uses as electrode materials in pharmaceutical catalysis, biosensors, rechargeable batteries, and in filtration systems, optoelectronic devices, water purification, and sophisticated magnetic materials. Piezoelectric devices, fuel cell electrodes, and other medical procedures also depend heavily on them. Additionally, their adaptability extends to biogenic and bioscience applications, where they support developments in medication delivery, diagnostic technologies, and biomedical research. Due to their potential to increase solar cell efficiency, MnO_x NPs have drawn considerable attention in the field of solar energy [6,7].

The development of synthesis techniques plays a pivotal role in determining the structural, functional, and application-specific characteristics of metal nanoparticles. For synthesizing nanoparticles with consistent size and shape. For synthesizing nanoparticles with consistent size and shape, traditional techniques such as laser ablation, which uses high-energy lasers to evaporate materials, solvo-thermal and hydrothermal processes, which involve reactions in solvents at high temperatures and pressures, and the sol-gel technique, a solution based chemical route that forms gel networks, are frequently used to synthesize the nanoparticles with consistent size and shape [8]. Despite their effectiveness, these methods have several significant problems, including high energy requirements, a reliance on hazardous solvents such as organic compounds like ethylene glycol, and the production of damaging by-products for the environment, such as greenhouse gases or acidic waste. Greener alternatives are required due to these issues, which limit their ecological sustainability and scalability [9].

To prepare nanoparticles, green synthesis processes utilize natural reducing and capping agents derived from plant extracts (such as neem and Aloe vera), microorganisms (including fungi, bacteria, and algae), and various solid wastes, such as spent mushroom compost, flower waste, coconut shells, wood waste, and other non-conventional plant residues. These biogenic techniques significantly minimize the environmental effect of nanoparticle manufacturing and assist to prevent ecological degradation. As a result, green synthesis has emerged as a sustainable and eco-friendly paradigm for preparing ZnO and other metal and metal oxide nanoparticles [9]. By introducing

bioactive surface functionalities, such as polyphenols or flavonoids from plant extracts, these environmentally friendly methods reduce toxic waste and energy consumption while improving antimicrobial efficacy through mechanisms like reactive oxygen species generation or membrane disruption and biocompatibility, which are essential for biomedical applications such as drug delivery or wound healing. Furthermore, by valuing renewable resources, green synthesis supports the ideas of the circular economy. Nanoparticle characteristics may be customized through precise control of synthesis factors. A few examples are temperature, which affects crystallinity and size (higher temperatures tend to produce smaller particles); pH, which affects shape (alkaline environments favor rods, while acidic conditions may produce spherical morphologies), precursor concentration, which controls particle growth rates; and reaction time for phase purity. This flexibility allows ZnO nanoparticles to be designed for a variety of uses, such as anisotropic forms for improved gas sensing, porous architectures for photocatalytic water treatment, or ultra-small particles for targeted cancer treatments. Scalable, environmentally friendly ZnO nanoparticle manufacturing may be advanced by researchers by balancing green chemistry and parameter optimization without sacrificing performance [5].

Zn-MnO composite nanoparticles enhance the performance of alkaline and Li-ion batteries by fusing the ZnO conductivity with the capacity of MnO. Flexible batteries have a better energy density with Zn-MnO cathodes. The novel structural Zn–MnO_2 composite battery based on carbon fiber demonstrated outstanding electrochemical performance and mechanical strength, making it extremely attractive for use in future structural energy storage applications [10]. Electron-hole recombination is decreased by the ZnO-MnO heterojunction. Envision solar-powered water purifiers using Zn-MnO, where Zn-MnO breaks down pesticides more effectively than individual oxides. Zn-MnO composites have a high sensitivity for detecting gases like ethanol and NO_2. Smart home sensors are also being proposed for detecting harmful vapors and sounding an alarm. Isam Abbas *et al.* prepared and investigated polypyrrole nanocomposites by mixing carbon nanotubes and ZnO, MnO, and MgO. They found that improvement in morphological and structural properties made them suitable for electronics and sensor applications [11]. The simultaneous ion release and ROS formation of Zn-MnO in wound dressings fight drug-resistant biofilms. According to EL-Moslamy *et al.*, Zn-MnO nanoparticles produced by microbes have antibacterial action against various bacteria and fungi [12]. Samy Selim *et al.* reported that a Zn-MnO nanocomposite can be used effectively to combat germs that are resistant to many drugs [13]. Zn-MnO utilizes the redox characteristics of both materials to enable quick charging in hybrid supercapacitors. The properties, applications, and eco-friendly approaches of ZnO and MnO nanoparticles motivated the synthesis of Zn-MnO composite nanoparticles using coconut shell through the Sol-Gel route, calcined at 450, 550, and 650 °C temperatures, and examined the efficacy and suitability of the synthesized nanocomposite in batteries, sensors or for biomedical applications. This work is the first to describe the green synthesis of Zn–MnO nanocomposites using *Cocos nucifera* shell extract. It shows how to create highly crystalline nanoparticles with adjustable crystallite sizes and unique optical absorption characteristics economically and sustainably. The nanocomposite has the potential to be used in optoelectronics, biosensing, and antimicrobial coatings due to its high optical conductivity, changeable surface charge, and exceptional

antibacterial and antifungal activity. The work is innovative and very distinct from previous ZnO or MnO green-synthesis research because of these combined properties.

Experimental

Materials

Coconuts were bought from supply stores in Hyderabad, Telangana, India. The outer layer, known as excerpt, and fiber husk were removed to yield the shell. The composition of dried coconut shell is cellulose (33.61%), lignin content (36.51%), pentosans (29.27%), ash (0.61%), and volatile matter (65–75%) [14]. Zinc nitrate hexahydrate [Zn $(NO_3)_2{\cdot}6H_2O$], manganous acetate ($C_4H_6MnO_4.4H_2O$), and liquor ammonia (NH_4OH) were procured from Sigma Aldrich with 99.9 % purity. Double-ionized distilled water and Whatman No. 1 filter paper were used to prepare the compounds as starting materials. Bacterial strains of *S. aureus*, *B. subtilis*, *P. aeruginosa*, and *E. coli* and fungal strains of *A. niger* and *Candida albicans* were obtained from the Vishnu Institute of Pharmaceutical Education & Research, Narsapur, Medak, Telangana, India.

Preparation of the extract of coconut shell powder

The raw coconut shell was gathered and cleaned to remove any impurities on the surface, such as soil particles or organic residues. Following the initial cleaning procedure, distilled water was used to verify that any remaining contaminants had been eliminated. After the coconut shell had been washed, it was allowed to air dry for 48 h at room temperature. The coconut shell was mechanically reduced in size using a large mortar and pestle for around 5-6 h after it had completely dried. The coconut shell gradually broke down into tiny pieces. A grinding machine was used to further grind the crushed material into a fine powder in order to produce a consistent distribution of particle sizes. The powdered material was then sieved through a 2 mm mesh to capture only particles of the required size for use in nanoparticle synthesis. Twenty-five grams of the powdered sample was mixed with 100 mL of deionized water (1:4) and boiled for 45 min with constant stirring. The mixture was then filtered with Whatman No. 1 filter paper to obtain the extract, which was stored in a refrigerator for further experimentation [9].

Synthesis of Zn-MnO composite nanoparticles using coconut shell powder extract

Zn-MnO composite nanoparticles were synthesized through the sol-gel method. The synthesis of Zn-MnO nanocomposite was carried out by adding 40 mL of coconut shell extract to 160 mL of 0.05 M zinc nitrate hexahydrate [Zn $(NO_3)_2{\cdot}6H_2O$] and 0.05 M manganous acetate ($C_4H_6MnO_4{\cdot}4H_2O$) in a ratio of 1:4 to make up the total volume to 200 mL. The solution was kept for stirring on a magnetic stirrer. The coconut shell aqueous extract contains phytochemicals (phenols, flavonoids, sugars, and tannins) that serve as reducing and capping/stabilising agents. Liquor ammonia was employed to adjust the pH of the solution to 10. The solution was boiled until it turned into a paste consistency. The paste was dried in an oven at 80 ℃ in platinum crucibles. This gentle heating or drying allows subsequent nucleation and growth of nanoparticles to form powder. The powder was divided into three parts and calcined for 3 h in a muffle furnace at 450, 550, and 650 ℃ before being allowed to cool. The resultant product was ground with a pestle and mortar. Zinc-manganese oxide nanoparticles (Zn-MnO) were obtained in powder form. The powder was subsequently placed in plastic vials for characterization. Figure 1 demonstrates the

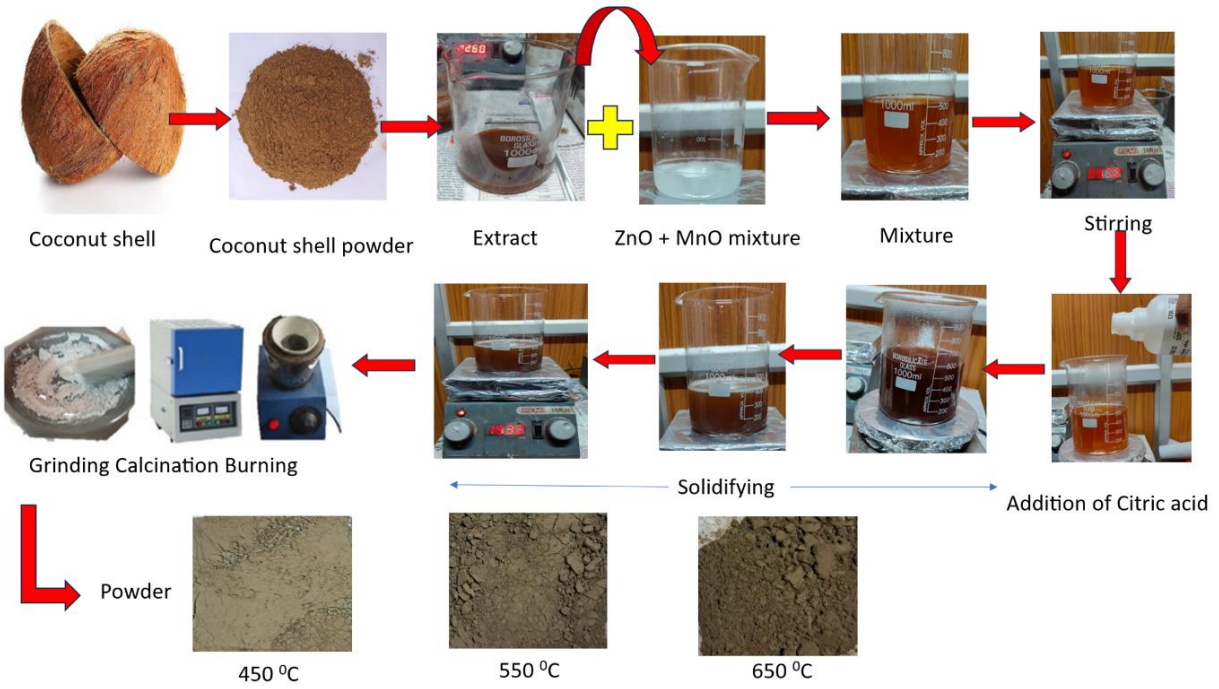

Figure 1. Synthesis process of Zn-MnO NPs from shell extract of *Cocos nucifera*

preparation steps for the Zn-MnO nanopowder. Hereafter, the compounds calcined at 450, 550, and 650 ℃ are labeled as ZM45, ZM55, and ZM65, respectively [4].

Characterization of compounds for structural and surface morphology studies

PANalytical, X'Pert powder diffractometer equipped with a Cu K_α source (λ = 1.54 Å) was used to determine the crystal structure of the prepared powders, and X-ray diffractometer **(**XRD) spectra were recorded at room temperature. Carl Zeiss Smart Field Emission Scanning Electron Microscope (FESEM) instrument was used to evaluate the morphology and elemental composition of the synthesized nano powders. Agilent Technologies Cary Series Ultraviolet-Visible-Near Infrared (UV–Vis-NIR) spectroscopy was used to record the optical absorption and bandgap features of the synthesized samples in the wavelength range of 200 to 800 nm.

The accuracy of the wavelength was ± 1 nm of the spectra. To evaluate the surface characteristics of the samples, the zeta potential of the samples was recorded using NanoPlus with NanoPlus AT (Auto Titrator). Fourier transform infrared (FTIR) spectra of the samples were recorded between 400 and 4,000 cm^{-1} using the JASCO-FTIR 4200 spectrometer. From these spectra, functional groups and bonding characteristics were examined. The KBr pellet method with a resolution of 0.7 cm^{-1} and an accuracy of 0.01 cm^{-1} was used to record FTIR spectra. The Raman spectra of the synthesized materials were recorded at room temperature using Horiba-micro-Raman and had a 532 nm He-Ne laser operating.

Antimicrobial activity

The antimicrobial efficacy of the three synthesized Zn-MnO nanocomposite samples calcined at different temperatures (450, 550, and 650 °C) was studied against both bacterial

strains and fungal strains. Antibacterial activity was tested against two Gram-positive bacteria (*S. aureus* and *B. subtilis*) and two Gram-negative bacteria (*P. aeruginosa* and *E. coli*), and antifungal activity was tested on two fungi (*A. niger* and *Candida albicans*). The agar well diffusion method determined the antimicrobial activity and minimum inhibitory concentration. The concentration of the sample used was 10% (100 mg/mL) against selected foodborne pathogens and spoilage microorganisms. Amoxicillin was used as drug standard at the concentration of 50 µg/mL, and dimethyl sulfoxide (DMSO) was the solvent used to dissolve the chemical moiety as a solvent control.

All three samples were further analyzed to determine their minimum inhibitory concentration (MIC). MIC evaluation was conducted using the agar well diffusion method by preparing serial dilutions of each sample at concentrations of 10% (100 mg/mL), 7.5% (75 mg/mL), 5% (50 mg/mL), 2.5% (25 mg/mL), and 1% (10 mg/mL). Wells (50 µL each) were loaded into agar plates inoculated with the respective test organisms, followed by pre-incubation diffusion at 4 ℃ for 1 h and subsequent incubation at 37 ℃ for 18 h.

Results and Discussion

X-ray diffraction studies

Figure 2 shows the XRD patterns of the Zn-MnO NPs calcined at 450, 550, and 650 ℃, which were coded as ZM45, ZM55, and ZM65. The observed peaks were approximately at 32°, 34°, 36°, 47.48°, 56.58°, 62.81°, 66.48°, 67.80°, and 69.14°, corresponding to the crystal planes (100), (002), (101), (102), (110), (103), (112), and (201). The sharp peaks indicated the crystalline nature of the compounds, which were

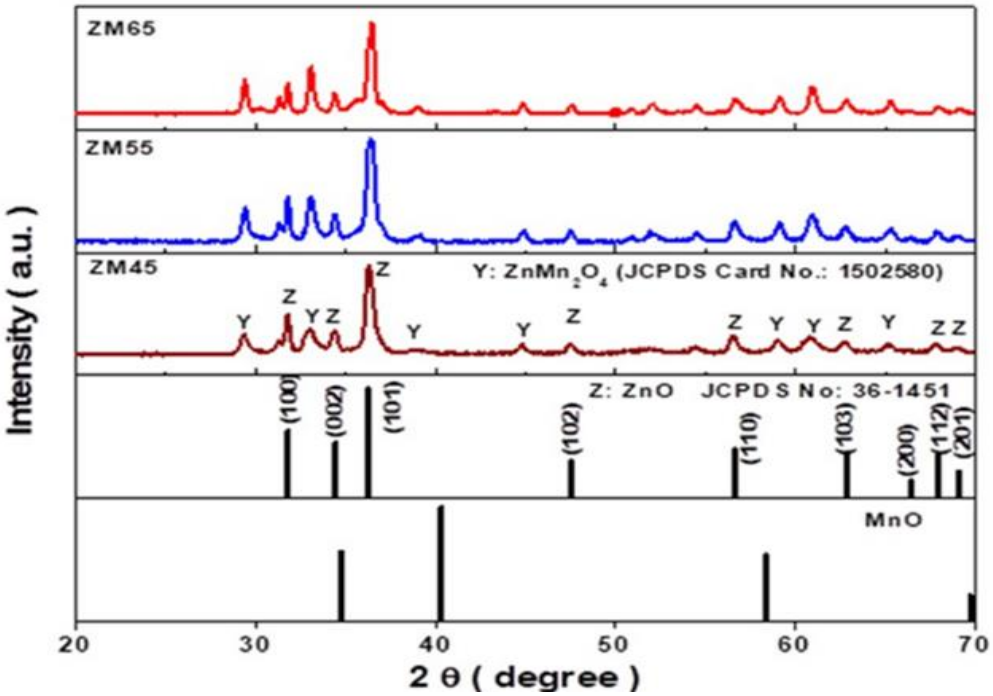

Figure 2. XRD patterns of Zn-MnO composite NPs calcined at 450, 550, and 650 ℃

in a hexagonal wurtzite crystal structure with the $P6_3mc$ space group. All these ZnO peaks are labeled with "Z" and their planes are represented with the corresponding Miller indices. There are a few minor secondary phases, labeled with "Y", due to the formation of the $ZnMn_2O_4$ phase. The XRD peaks of both the phases were compared with JCPDS data, as depicted in Figure 2 and the literature [15,16]. With the increase in calcination temperature, the XRD peaks were found to be sharper, indicating improved crystallinity of the compounds which in turn decreased the full-width at half-maximum values.

The crystallite sizes (D) of the compounds were calculated using Scherrer's formula as given by Equation 1 [15].

$$D = \frac{k\lambda}{\beta \cos\theta} \quad (1)$$

Where, k is a constant (0.89), λ is the wavelength of the X-rays used (0.154 nm), θ is the diffraction angle of a maximum intensity peak, and β is the full width at half maxima [15]. The crystallite sizes of ZM45, ZM55, and ZM65 were 15, 16, and 19 nm, respectively.

It clearly indicated that the calcination temperature increased the crystallite size of the compounds. Smaller crystallites have a higher surface area to volume ratio, leading to higher surface energy. At elevated temperatures, atoms can migrate more easily to reduce this surface energy by joining with larger crystallites [16].

Scanning electron microscopy and energy dispersive X-ray spectroscopy

Figure 3 shows the SEM micrographs of the compounds. It revealed that at 450 ℃, the particles had an uneven shape and seemed less crystalline [17]. Less clear grain boundaries suggested insufficient development. The particles nevertheless exhibited a porous structure despite some aggregation. In contrast to 450 ℃, the particles at 550 ℃ were more homogeneous and had more distinct forms. Grain size was bigger, and enhanced crystallinity was evident, suggesting an increase with temperature. Some loose aggregation, but less porosity than at 450 °C was observed. At 650 °C, because of grain coalescence and sintering at higher temperatures, the particles were noticeably bigger. Dense packing and fewer permeable areas were seen in the morphology. Structures became more compact and crisper with clear crystallite development. Grain development and crystallinity were enhanced by raising the calcination temperature, which was consistent with thermal energy promoting crystallite coalescence. This trend supports the findings of XRD, which showed increased crystallinity with temperature as seen from sharper peaks.

Particle size was measured by employing image software, according to which the average particle size increased from 66 (ZM 45) to 86 (ZM 55) and 136 nm (ZM 65) as a result of calcination. Nanoparticles were smaller and less ordered at 450 °C, making them suitable for large surface-area applications such as adsorption, catalysis, etc. Particle size and crystallinity were balanced at 550 ℃, making it appropriate for optical and electrical applications. Particles were larger and less porous at 650 °C, but they were more crystalline; this makes them ideal for applications that need stability, such as ceramics and sensors.

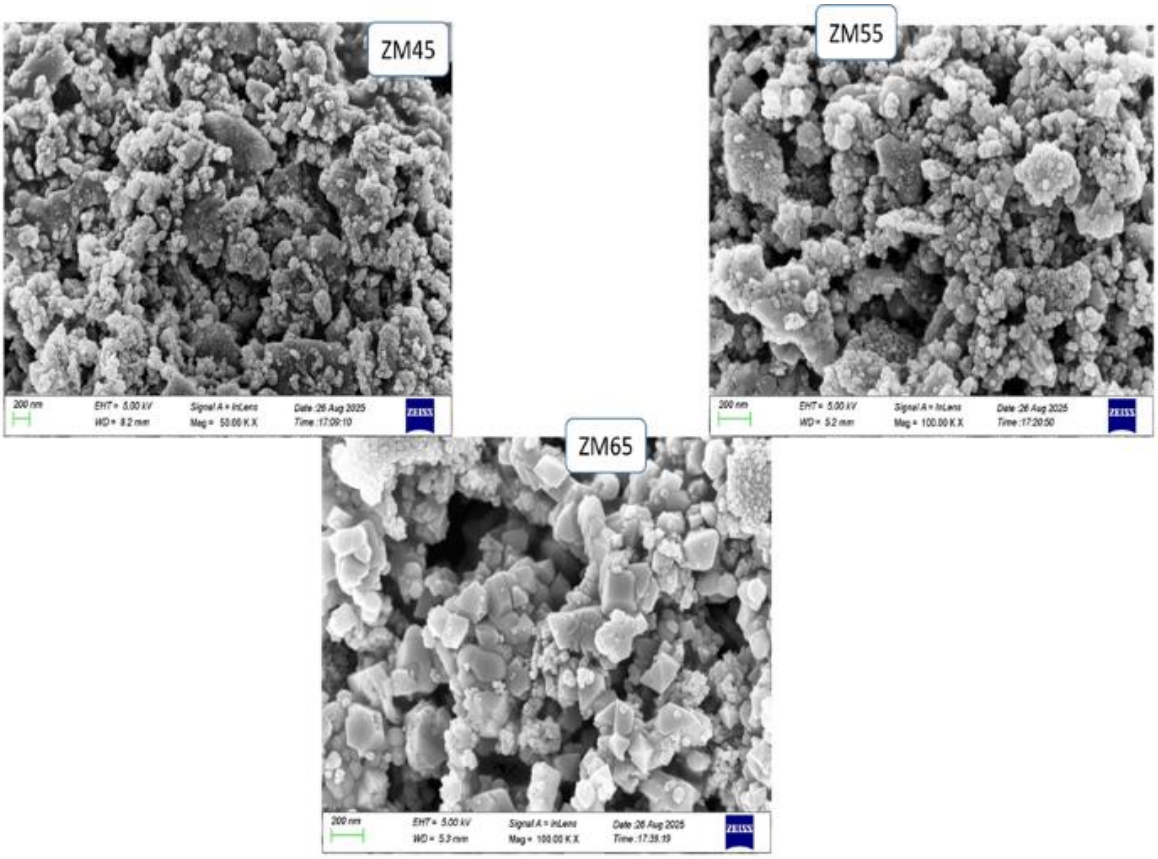

Figure 3. SEM images of ZM45, ZM55, and ZM65 compounds

EDS analysis, shown in Figure 4, visualized the presence of Zn and Mn with a roughly equiatomic cation ratio (Zn: Mn = 1:1) in all samples ZM45, ZM55, and ZM65. Zn content slightly decreased from 44.16 wt% at 450 °C to 41.90 wt% at 650 °C, Mn content decreased from 39.52 to 38.58 wt%, whereas oxygen content increased from 16.32 to 19.52 wt%. Improved oxide formation and a decrease in surface adsorbates were likely the causes of the greater oxygen weight % at 650 °C [13]. If spinel $ZnMnO_4$ was present, it was likely a small secondary phase. The EDS, in conjunction with SEM (grain coarsening and densification with temperature) and XRD (peak sharpening), confirmed the creation of a Zn–Mn–O composite with minimal extraneous impurities. These spectra allowed clean synthesis since they do not include any notable impurity elements such as Na, Cl, or Si.

Optical studies

UV -Vis spectroscopy

UV–Visible spectroscopy was used to characterize the optical properties of Zn-MnO composite NPs. To determine the influence of calcination temperature on the optical properties of Zn-MnO composite nanoparticles, the UV-Visible spectra in the 200–800 nm region were recorded and are shown in Figure 5. Peculiar peaks were visible in the spectra with slight variation, at 272, 278, and 288 nm for Zn-MnO NP samples ZM45, ZM55, and ZM65, respectively. Different positions of the absorption bands indicated that different morphologies and size variations were present

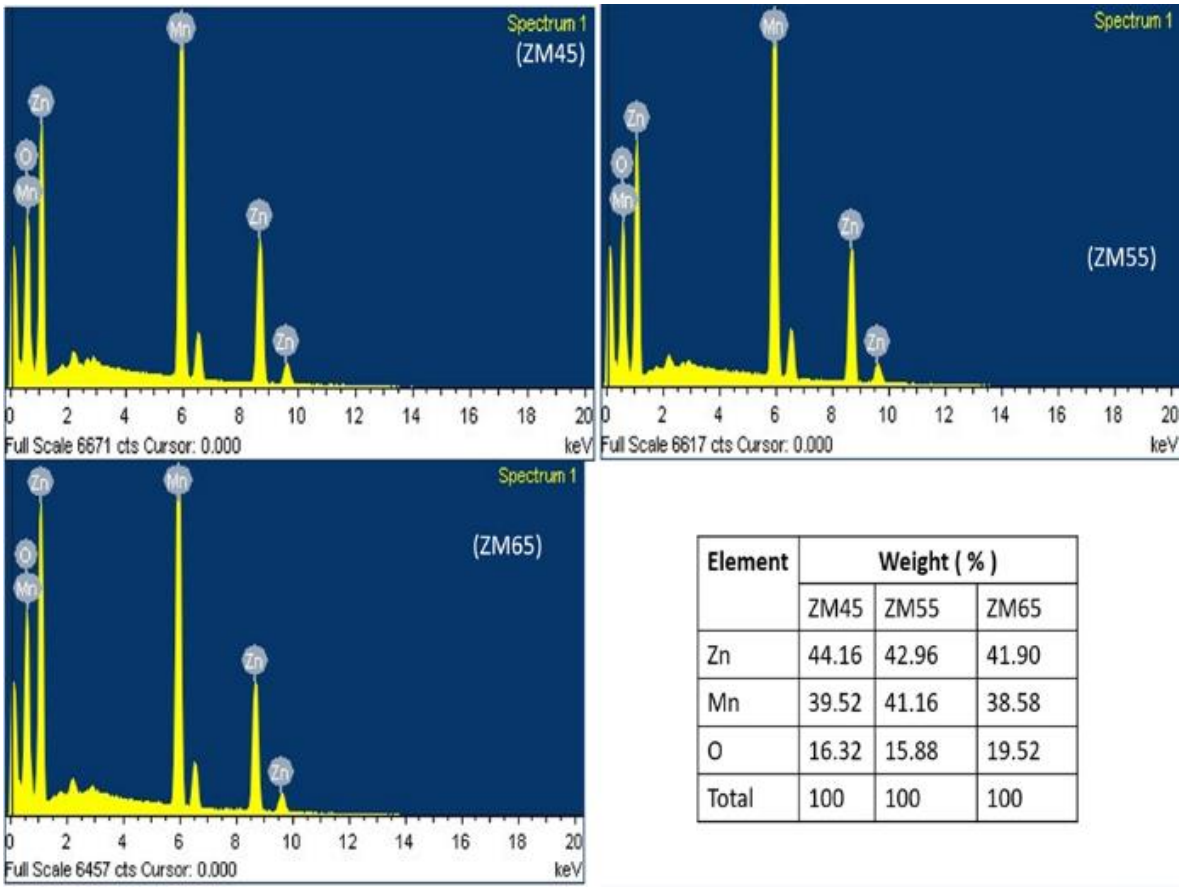

Element	Weight (%)		
	ZM45	ZM55	ZM65
Zn	44.16	42.96	41.90
Mn	39.52	41.16	38.58
O	16.32	15.88	19.52
Total	100	100	100

Figure 4. EDS images of ZM45, ZM55, and ZM65 compounds

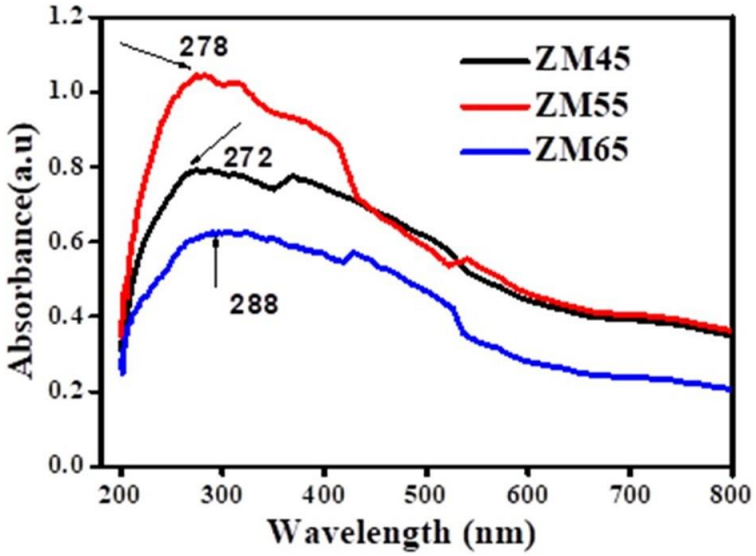

Figure 5. UV-Vis spectra of Zn-MnO composite NPs: ZM45, ZM55, and M65

[18]. The results of the UV-Vis investigation were in excellent alignment with earlier research [16,19,20]. Low long-wavelength absorption values compared to the absorption peak of bulk ZnO were found between 300 and 400 nm, and of bulk MnO were found between 350 and 410 nm [21,22], which were caused by impurities in Zn-MnO NPs, such as oxygen vacancies that serve as donor defects. For the rise in calcination temperature, the peak of absorption was pushed to a longer wavelength from 272 to 288 nm. Qualitatively, it was demonstrated that raising the calcination temperature increased crystallite size, reduced quantum confinement effects, and may have stabilized or rearranged the oxygen vacancies, which resulted in lowering the bandgap energy [23]. Thus, nanoparticles that show an absorption peak at a lower wavelength are smaller than those that show a peak at a higher wavelength. This is consistent with the particle size determined using Scherrer's formula. From the absorption spectra of Zn-MnO composite nanoparticles, the energy gap can be obtained by the Tauc's relation represented by Equations 2 and 3 [24].

$$\alpha h\upsilon = B\left(h\upsilon - E_{Opt}\right)^{n} \quad (2)$$

Where α is the absorption coefficient at the frequency of ν. α = 2.303 A/t, where A is absorption and t is sample thickness. For direct permitted transitions of n = ½, therefore, the above equation is reduced as Equation 3 [24]:

$$\alpha h\upsilon = B\left(h\upsilon - E_{Opt}\right)^{1/2} \quad (3)$$

The optical bandgap energy E_{opt} values were obtained by extrapolating the linear portion of the $(\alpha h\upsilon)^2$ versus hν curve and finding the intercept on the energy axis [25]. The optical bandgap energies were estimated by Tauc plots for Zn-MnO nanoparticles made using coconut shell extract in an environmentally friendly manner and are depicted in Figure 6. The trend in bandgaps was 2.458 eV, 2.406 eV, and 2.130 eV for ZM45, ZM55, and ZM65 samples, respectively. Higher synthesis temperatures caused the bandgap to decrease, indicating structural or electrical changes. In the investigation conducted by Haowei Peng *et al.* on $Mn_{1-x}Zn_xO$ alloys, the bandgap was found to be 2.30 eV, which was within the range of the bandgap calculated in the present work [26]. Extract from coconut shells served as a reducing and capping agent. Organics from coconuts broken down at higher temperatures have minimized surface flaws or carbonaceous coatings that might have artificially decreased E_g. Cleaner structures and surfaces resulted in inherent bandgaps.

Refractive index

One essential characteristic of optical materials crucial for constructing optical devices is the refractive index (n). Therefore, regulating this characteristic in polymers and nanoparticles enables their practical use in several industrial and medicinal applications. The bandgap value may be used to determine the empirical connection that applies to various types of molecules. The refractive index was calculated using Equation 4 [27].

$$n = \sqrt{\frac{12.417}{\sqrt{E_g - 0.365}}} \quad (4)$$

Values calculated for ZM45, ZM55, and ZM65 were 2.930, 2.948, and 3.057, respectively.

Optical conductivity

The capacity of a substance to conduct or absorb light in response to an applied electromagnetic field is measured by its optical conductivity. It is an important parameter,

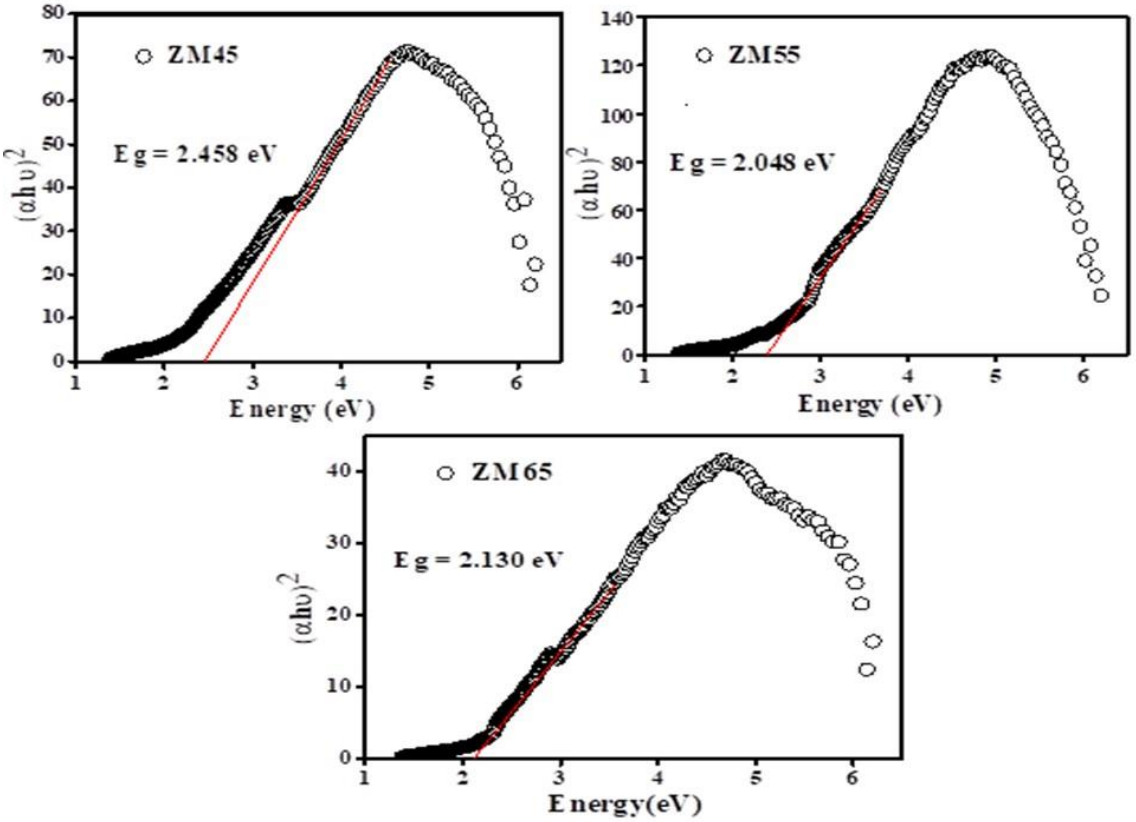

Figure 6. Tauc's plots of Zn-MnO composite NPs: ZM45, ZM55, and ZM65

especially for nanomaterials, to understand how light interacts with matter. The optical conductivity of nanoparticles is influenced by several parameters, including their size, shape, material composition, and surrounding environment. Surface plasmon resonance (for metallic nanoparticles) and quantum confinement effects allow nanoparticles to display unique optical features. Utilising the absorption coefficient α and the refractive index 'n' data, the optical conductivity $\boldsymbol{\sigma_{opt}}$ for all the samples was computed using the subsequent relation shown in Equation 5 [28].

$$\sigma_{opt} = \frac{\alpha n c}{4\pi} \quad (5)$$

Where, the absorption coefficient $\alpha = \frac{2.303 \times A}{t}$ (A denotes absorbance and t is thickness of the sample 1 cm) and c is the velocity of light.

The optical conductivity values of samples are shown in Table 1. The ZM55 sample had the highest optical conductivity, 2.466×10^{9} S^{-1}, compared to ZM45 and ZM65 samples. A material characterized by a high absorption coefficient can absorb a greater amount of light, typically suggesting that a larger portion of the light energy can be transformed into electric current, thereby enhancing the optical conductivity. Furthermore, a material possessing a higher refractive index will significantly influence light propagation, potentially improving the interaction between the light and the material's electrons, which in turn can further elevate optical conductivity. Materials with strong optical conductivity are capable of efficiently converting light into electrical energy.

Table 1. Optical parameters of Zn-MnO nanoparticles at different calcination temperatures

Sample code	Absorption peak wavelength $\lambda_{(max)}$ (nm)	Energy gap E_g (eV)	Refractive Index n	Optical conductivity σ_{opt} ($\times 10^9 s^{-1}$)
ZM45	272	2.458	2.930	1.852
ZM55	278	2.406	2.948	2.466
ZM65	288	2.130	3.057	1.541

Zeta potential

The term "zeta potential" describes the electrical potential at a solid surface's sliding plane when it comes into contact with a liquid, usually water. It indicates the strength of the repulsion between nearby, similarly charged particles in dispersion. It is an essential parameter for describing the surface charge of colloidal systems or nanoparticles and is crucial for understanding the stability of foams, emulsions, and colloids [29]. As an interfacial property, the zeta potential is affected by the pH and content of the surrounding liquid medium in addition to the physicochemical characteristics of the solid surface [30]. A solid surface usually gains a surface charge when submerged in an aqueous environment due to the ionization of surface groups or the adsorption of liquid ions. An electrical double layer (EDL) is created when oppositely charged ions from the surrounding medium are drawn to this charged surface.

The stern layer, a firmly bonded layer of counter ions, and the more diffuse outer layer make up the EDL [31]. The zeta potential is the potential at the interface between the diffuse and stern layers. Higher absolute values (positive or negative) indicate stronger repulsion between particles, which prevents aggregation. This potential is frequently employed as a measure of colloidal stability [32]. At various calcination temperatures, the surface charge of the produced nanoparticles was evaluated for the current zeta potential analysis. Suspensions displaying 15 mV were classified as stable colloids [33]. Zeta potential values for samples ZM45, ZM55, and ZM65 were determined to be -9, -10, and 16 mV, respectively, as shown in Figure 7. Changes in surface morphology or charge distribution on the nanoparticle surface may be the cause of the temperature-dependent rise in zeta potential, which might indicate improved surface activity or dispersion stability at higher calcination temperatures.

Fourier transform infrared (FTIR) spectra

Fourier transform infrared spectroscopy is considered as the best technique for discerning the structure and properties of materials, offering insights into their chemical groups. Figure 8 illustrates the FT-IR transmittance spectra in the 200-800 cm^{-1} of Zn-MnO composite nanoparticles mediated by coconut shell at 450, 550, and 650 ℃. The small band seen in the range of 3,431–3,684 cm^{-1} and a peak in the range 1,630–1,640 cm^{-1} can be attributed to the stretching and bending O–H vibrations of adsorbed H_2O molecules that were adsorbed on the surface of the nanocomposites, resulting from their porosity [34-36]. The disappearance of the 1,631 cm^{-1} peak with increasing temperature was mostly due to thermal breakdown or desorption of surface-bound organic compounds originating from plant extracts or biological sources [37]. The amide II mode was represented by the FTIR absorption band seen at 1,535 cm^{-1}, which was primarily involving N–H bending and C–N stretching

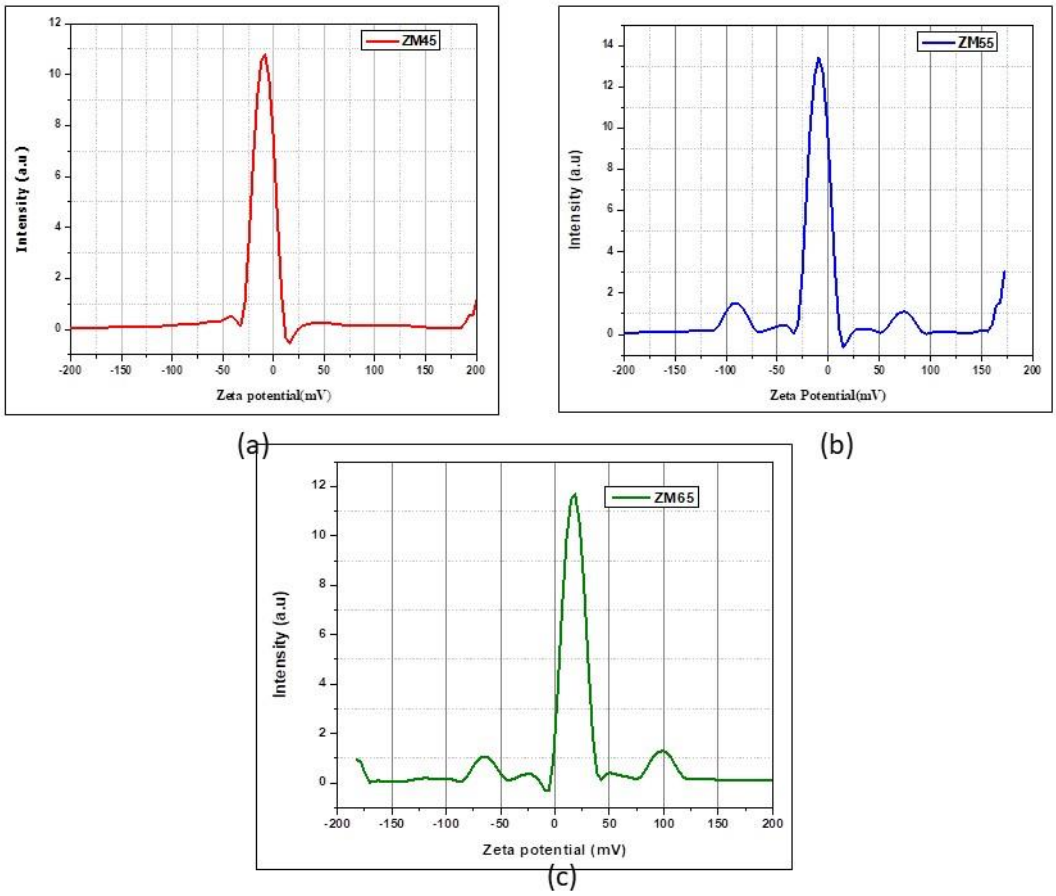

Figure 7. Zeta potential of Zn-MnO NPs: (a) ZM45, (b) ZM55, and (c) ZM65

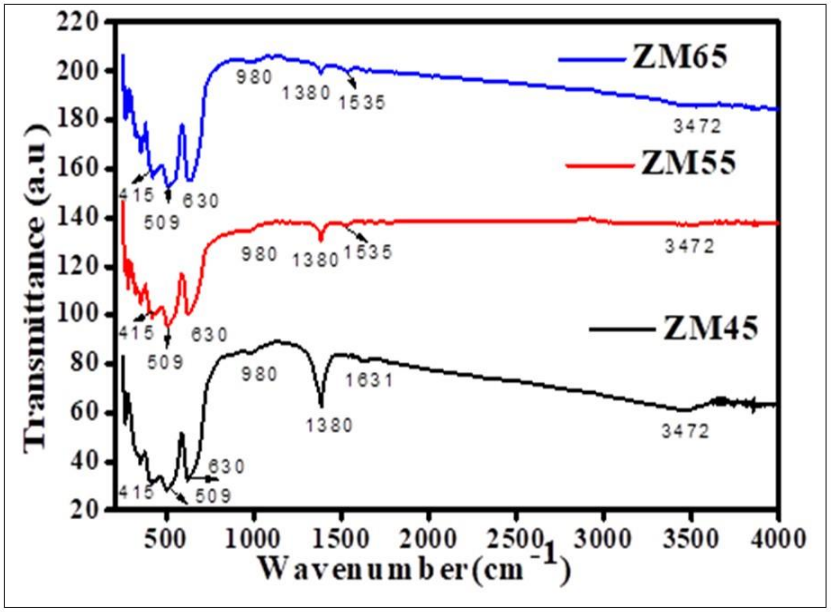

Figure 8. FTIR spectra of Zn-MnO NPs: ZM45, ZM55, and ZM65

vibrations. Its existence suggested that Zn–MnO nanoparticles have interacted with organic substances containing nitrogen, including proteins or amino acid residues, which were likely the products of biological agents utilized in synthesis. These interactions implied that biomolecules were successful in capping or surface functionalizing the nanoparticles [38]. The transmittance peak, whose intensity decreased with temperature at approximately 1,380 cm^{-1} was due to C-C stretching bonds, suggesting aromatic compounds, while N-O symmetric stretching indicated nitro compounds [39]. Aromatic rings and nitro groups may start to decompose or change chemically (oxidation, rearrangement, etc.) at high temperatures. As a result, the strength of IR transmittance at that particular frequency was decreased. The 980 cm^{-1} band was ascribed to C-O-C stretching vibrations, which were indicative of ether bonds widely seen in proteins and polysaccharides [40]. The absorption band at 630 cm^{-1} in the FTIR spectrum was attributed to the vibrational mode of Zn-O bonds within the ZnO nanoparticles. This suggested that the ZnO nanoparticles were likely interacting with surrounding organic moieties, such as phytochemicals or capping agents, which possibly present on their surface due to the synthetic technique [41]. In the 400 to 600 cm^{-1} wavenumber range, the distinctive absorption bands were visible in the fingerprint region of the metal-oxygen bonds [42]. All the anomalies are listed in Table 2.

Raman spectral analysis

Raman spectral analysis elucidates chemical structure, phase, crystallinity, and interaction between molecules. The spectra, spanning the 200–1,100 cm^{-1} range, capture both higher-wavenumber molecular characteristics brought on by organic residues, surface adsorbates, or hydroxyl groups and lattice vibrations (Raman active phonon modes). The intensity rises as the calcination temperature rises, suggesting greater phonon coupling and improved crystallinity. Zn–MnO nanoparticles ZM45, ZM55, and ZM65, calcined at 450, 550, and 650 °C showed different phonon modes linked to Zn–O and Mn–O bonding in their Raman spectra, as shown in Figure 9 and the deconvoluted peaks, as indicated in Figure 10. All the obtained peaks are tabulated in Table 3. A peak was observed at 296 cm^{-1}, which was assigned to B_1^{high} – B_1^{low} bending vibrational modes, a similar kind of peak was seen at 297 in Mn-doped ZnO, was reported [43]. The faint peak appearing at approximately 332 cm^{-1} could be related to the (E2 (high)-E2 (low)) multi-phonon scattering mechanism. It was observed that the peak shifted from 336 to 347 cm^{-1} with an increase in calcination temperature. This blue shift often indicates compressive stress in the lattice [44].

The E_2(high) Raman mode at approximately 432 cm^{-1} was mainly related to the vibration of oxygen atoms in the wurtzite of ZnO. It is well-regarded as a mark of high crystallinity. With increasing calcination temperature to 650 °C, a red shift of E_2(high) was observed from 432 cm^{-1} to 414 cm^{-1}. This is because particle growth would lead to the Zn-MnO composite or mixed oxide phase [45]. The peak at approximately 506 cm^{-1} was due to multi-phonon scattering modes corresponding to E_1(TO)+E_2(LO) of ZnO [46]. The peak at approximately 530 cm^{-1}, corresponding to the A1(LO) mode in wurtzite-structured ZnO, shifted to approximately 545 cm^{-1} upon calcination at higher temperatures, suggesting better crystalline ordering [16].

Table 2. FTIR band positions of Zn-MnO NPs

Band position (cm^{-1})	Band assignment	Ref.
~ 415 and 509	Fingerprint region of the metal-oxygen bonds	[42]
~ 630	Vibrational mode of Zn-O bonds within the ZnO nanoparticles	[41]
~ 980	Ascribed to C-O-C stretching vibrations, which are indicative of ether bonds widely seen in proteins and polysaccharides	[40]
~ 1,380	due to C-C stretching bonds, suggesting aromatic compounds, while N-O symmetric stretching indicates nitro compounds	[39]
~ 1,535	N–H bending and C–N stretching vibrations	[38]
~ 1,631 and ~ 3,472	Stretching and bending O–H vibrations of adsorbed H_2O molecules	[37] [34-36]

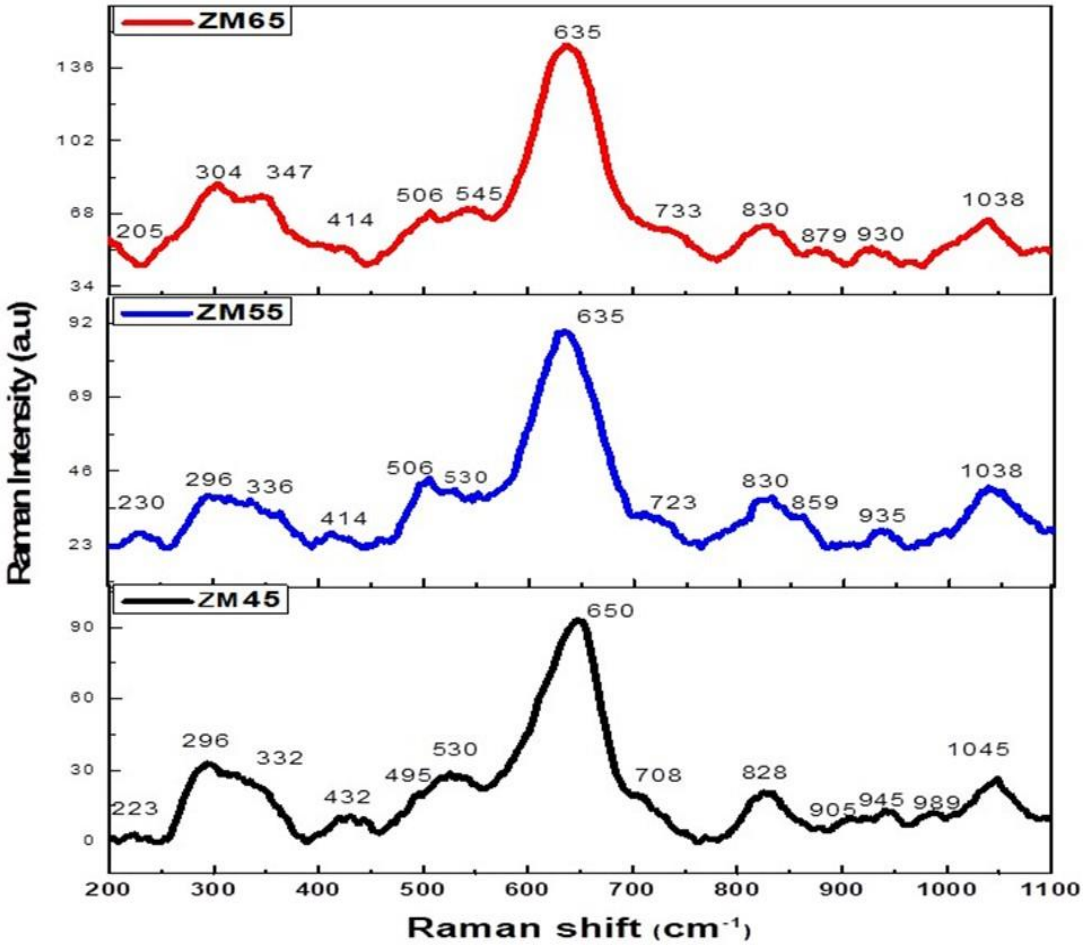

Figure 9. Raman spectra of Zn-MnO NPs: ZM45, ZM55, and ZM65

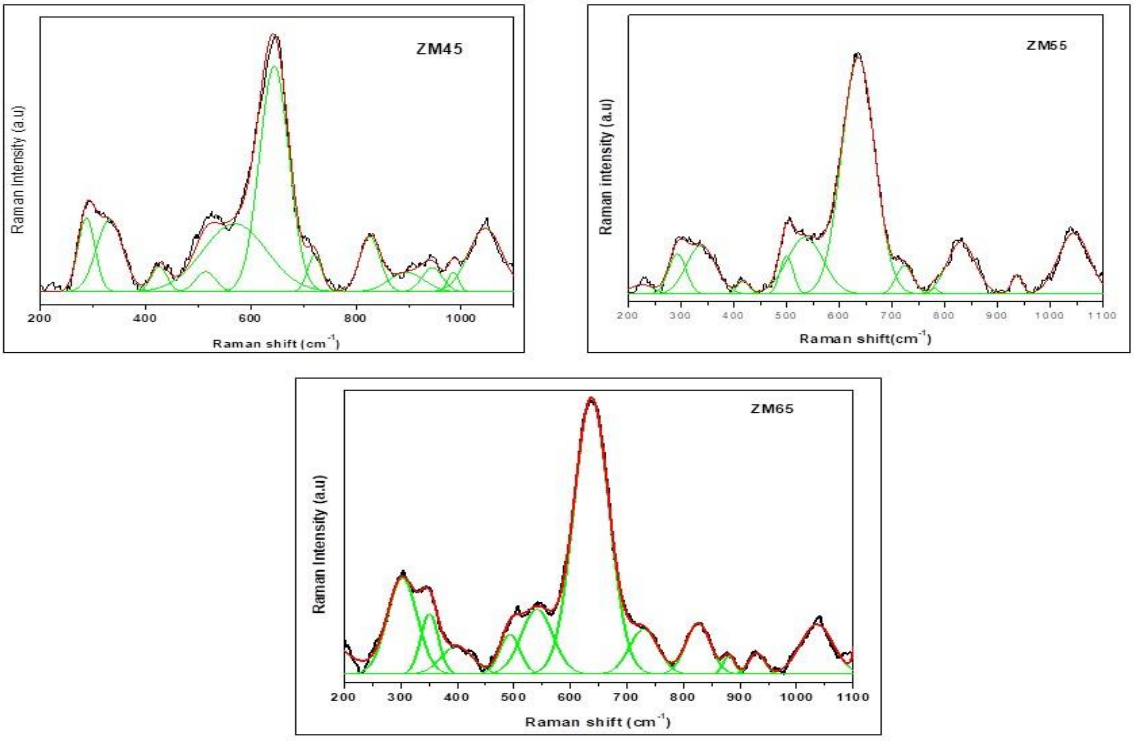

Figure 10. Raman deconvolution spectra of Zn-MnO NPs: ZM45, ZM55, and ZM65

Table 3. Raman band positions and their assignments of Zn-MnO NPs

Band position (cm^{-1})			Band assignment	Ref.
ZM45	ZM55	ZM65		
296	296	304	Is assigned to $B_1^{high} - B_1^{low}$ bending vibrational modes	[43]
332	336	347	Related to the (E2 (high)-E2 (low)) multi-phonon scattering mechanism.	[44]
432	414	414	The E_2(high) Raman mode is associated with oxygen atom vibrations in ZnO	[45]
495	506	506	The multi-phonon scattering modes of ZnO $E_1(TO)+E_2L$	[46]
530	530	545	Corresponding to the A1(LO) mode in wurtzite-structured ZnO	[16]
650	635	635	Vibration modes attributed to substances containing magnesium.	[47,48]
708	723	733	A_1 symmetry secondary Raman modes	[48]
828	830	830	These are attributed to dioxygen species adsorbed or incorporated in the ZnO lattice.	[49]
905	859	879		
945	935	930		
989	-	-		
1.045	1.038	1.038	A two-phonon Raman scattering event, where $A_1(TO)$ and $A_1(LO)$ phonons were combined.	[50]

Vibration modes at approximately 650 cm^{-1} were attributed to substances containing Mn. With calcination temperature, a red shift to approximately 635 cm^{-1} was observed; this might be due to oxygen loss, which leads to reduced Mn oxidation state from Mn^{4+} to Mn^{3+} or Mn^{2+} [47]. In the intermediate region of the spectrum, the second-order Raman mode with A_1 symmetry (~723) was observed [48].

Raman peaks with wide, less-resolved bands in the 800–1,000 cm^{-1} area were found in Mn-doped ZnO or Zn–MnO composites or in defect-rich materials, where oxygen vacancies and local charge imbalances are more prominent. These bands were attributed to dioxygen species adsorbed or incorporated in the ZnO lattice. The peroxide ion (O_2^{2-}) was stabilized in the ZnO lattice, displaying a stretching mode close to approximately 840 cm^{-1} [49]. The peak at approximately 1,050 cm^{-1} was caused by a two-phonon Raman scattering event, where A_1(TO) and A_1(LO) phonons combine. This interaction was permitted by group theory at the A and H locations in the Brillouin zone of the hexagonal lattice of ZnO. The Raman peak 1,050 cm^{-1} shifted to 1,038 cm^{-1} with increasing calcination temperature. This shift may be due to oxygen vacancies, which are more prevalent in Zn–MnO nanoparticles at low temperatures. The defect density decreased with calcination. The ZnO lattice reduced distortion by segregating into secondary phases such as MnO_2 [50].

The synthesized Zn-Mn oxide (Zn-MnO) NPs in three samples, ZM45, ZM55, and ZM65 that were calcined at 450, 550, and 650 °C, respectively, each at a concentration of 10% (w/v) were tested for their antimicrobial activity against selected food-borne pathogens and spoilage microorganisms using the agar well diffusion method, as depicted in Figure 11 [51,52].

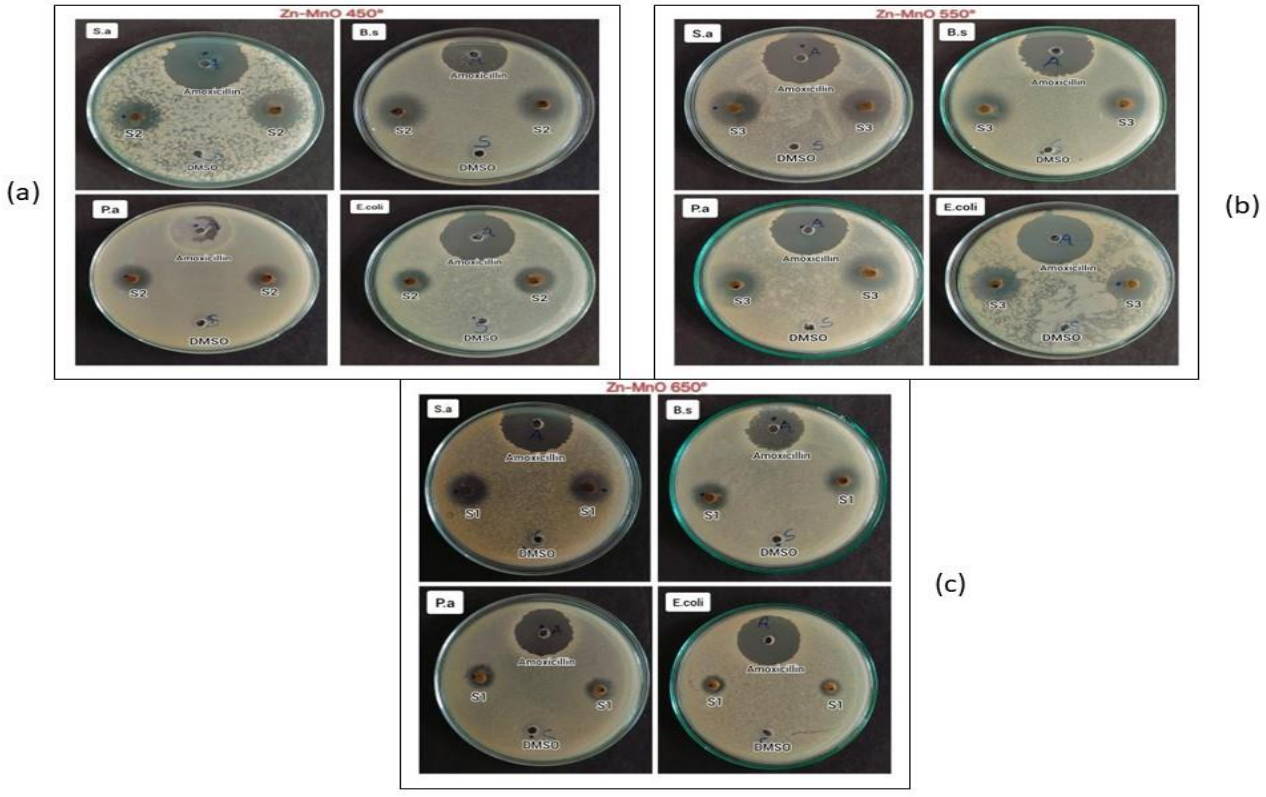

Figure 11. Inhibition zones of Zn-MnO nanocomposite NPs: (a) ZM45, (b) ZM55, and (c) ZM65, tested on bacteria *S. aureus, B. subtilis, P. aeruginosa*, and *E. coli*

Antimicrobial activity

Metal nanoparticles that were synthesised through the green route have shown antibacterial activity at concentrations greater than 100 mg/mL [53]. Compared to their chemically manufactured counterparts, metal nanoparticles that are biogenically formed have demonstrated a higher antibacterial activity. The inclusion of proteins and other macromolecules in the capping agents obtained from biological sources is thought to be responsible for this increased activity, as it may improve their ability to interact with microbial cells [54]. According to several studies, the production of reactive oxygen species (ROS) and the release of metal ions (Zn^{2+} and Mn^{2+}) were the main causes of the antibacterial activity of Zn-MnO composite nanoparticles against bacterial species. These ROS, which were created when the nanoparticles interacted with their surroundings, comprised hydrogen peroxide (H_2O_2), hydroxyl radicals (-OH), and superoxide ions (O_2^{-2}). Because the Zn and Mn components worked in concert, the Zn-MnO nanocomposite promoted increased ROS production. Since manganese is a redox-active metal, it can cycle between the Mn^{2+}, Mn^{3+}, and Mn^{4+} oxidation states, which further increased oxidative stress in bacterial cells. Once produced, the ROS interact with the negatively charged bacterial cell membranes through the release of Zn^{2+} and Mn^{2+} ions. The integrity of the membrane was compromised by this contact, increasing permeability and allowing intracellular contents to seep out. Cell lysis and bacterial death followed the loss of vital macromolecules from the cell [55]. All the Zn-MnO samples showed significant zones against both the microorganisms, specifically bacterial as well as fungal strains, inferring broad-spectrum antimicrobial action, as seen in Tables 4 and 5. Such activity was observed earlier in Zn-MnO nanocomposites [56,57].

Among the three, the Zn-MnO sample ZM65 showed the most pronounced antibacterial activity, indicating that higher calcination temperature may enhance the antimicrobial potency of Zn-MnO nanoparticles. For *S. aureus*, the inhibition zone diameter was maximum (22 mm) compared to the others. The next highest inhibition zone diameter (18 mm) was for *E. coli*. Notably, there was no calcination effect on the inhibition zone diameter for above two strains. The inhibition diameter against *P. aeruginosa* was increased from 13 mm to 18 mm, whereas for *B. subtilis* it decreased from 17 mm to 15 mm with calcination temperature of 450-650 ℃. The inhibition zone for fungi was maximum as 19 mm for *A. niger* for the sample ZM55 and 17 mm for *Candida albicans* [6].

Table 4. Antibacterial activity of Zn-MnO NPs

S. No.	Sample code		*E. coli*	*P. aeruginosa*	*S. aureus*	*B. subtilis*
			Inhibition zone diameter (mm)			
1	ZM45	Amoxicillin	26	24	27	24
		DMSO	8	8	8	8
		Sample	18	13	22	17
2	ZM55	Amoxicillin	26	25	26	27
		DMSO	8	8	8	8
		Sample	17	18	22	15
3	ZM65	Amoxicillin	26	24	24	25
		DMSO	8	8	8	8
		Sample	18	18	22	15

Table 5. Antifungal activity of Zn-MnO NPs

S. No.	Sample code		*Candida albicans* Inhibition zone diameter (mm)	*A. niger*
1		Itraconazole	21	22
	ZM45	DMSO	9	8
		Sample	16	14
2		Itraconazole	23	22
	ZM55	DMSO	8	8
		Sample	17	19
3		Itraconazole	20	20
	ZM65	DMSO	8	8
		Sample	17	15

All three samples were further analyzed to determine their minimum inhibitory concentration. MIC was defined as the lowest concentration at which visible microbial growth was inhibited. All experiments were carried out in duplicate. MIC data, as depicted in Tables 6 and 7, revealed that all samples effectively inhibited bacterial growth at 2.5% and fungal growth at 5% concentrations. The minimum inhibitory concentration for bacterial strains, *S. aureus* was 2.5% for three samples, and for *E. coli* and *B. subtilis* was 5%. MIC for *P. aeruginosa* was 7.5%, which was high when compared to other strains. In the case of fungi *Candida albicans* and *A. niger*, the MIC was 5% for the samples calcined at ZM55. For the other samples, it was 7.5%.

Table 6. MIC of Zn-MnO against bacteria

Sample code	Name of the organism	Concentration				
		1%	2.5%	5%	7.5%	10%
		Inhibition zone diameter (mm)				
ZM45	*E. coli*	-	-	13	16	18
	P. aeruginosa	-	-	-	11	13
	S. aureus	-	11	16	18	22
	B. subtilis	-	-	12	14	17
ZM55	*E. coli*	-	-	14	16	17
	P. aeruginosa	-	-	-	14	18
	S. aureus	-	12	15	19	22
	B. subtilis	-	-	-	13	15
ZM65	*E. coli*	-	-	12	15	18
	P. aeruginosa	-	-	-	16	18
	S. aureus	-	12	14	18	22
	B. subtilis	-	-	-	12	15

Table 7. MIC of Zn-MnO against fungi

Sample Code	Name of the organism	Concentration				
		1%	2.5%	5%	7.5%	10%
		Inhibition zone diameter (mm)				
ZM45	*Candida albicans*	-	-	-	13	16
	A. niger	-	-	-	10	14
ZM55	*Candida albicans*	-	-	11	15	17
	A. niger	-	-	12	14	19
ZM65	*Candida albicans*	-	-	-	14	17
	A. niger	-	-	-	12	15

Conclusion

Cocos nucifera shell-mediated synthesis successfully produced Zn–MnO composite nanoparticles with minor $ZnMn_2O_4$ secondary phases. Increasing calcination temperature enhanced crystallinity, particle size, and structural ordering, as confirmed by XRD and Raman analysis. UV–Vis results showed a progressive narrowing of the bandgap from 2.458 to 2.130 eV, due to the removal of organic residues and reduced surface defects. The rise in zeta potential (-9, -10, and 16 mV) with temperature indicated improved dispersion stability and surface activity. FTIR confirmed bonding with nitrogen-containing biomolecules, suggesting an active role of biological agents in nanoparticle stabilization. Raman spectra confirmed multiple Mn oxidation states and better crystalline ordering at higher calcination. Antimicrobial studies revealed temperature-dependent effects. Antimicrobial activity against *P. aeruginosa* improved from 13 mm to 18 mm diameter, while that against *B. subtilis* slightly declined (17 mm to 15 mm diameter); *S. aureus* showed strong inhibition at 2.5% MIC. Overall, calcination temperature played a crucial role in tuning the structural, optical, and antimicrobial properties of biogenic Zn–MnO nanocomposites.

Acknowledgments

The authors would like to thank the Head of Department of Sciences & Humanities, Principal and Management of Matrusri Engineering College (Autonomous), Saidabad, Hyderabad, Telangana, India, for providing the necessary facilities and financial support to carry out this work.

Conflict of Interest

No potential conflict of interest was reported by the authors in this work.

Funding

None.

Data Availability

Data will be made available on request.

ORCID

Chandrasekhar Maalegoundla
https://orcid.org/0000-0002-6395-7403
Naveen Pusapati
https://orcid.org/0009-0002-7773-3563
Lakshmi Satya Boddu
https://orcid.org/0000-0002-1091-1620
Pavan Kumar Naini

https://orcid.org/0000-0002-1040-8064
Sowmyya T
https://orcid.org/0000-0003-0644-8992

References

[1] Ali, I., Rahman, A. Environmental degradation: Causes, effects and solutions. *International Journal for Multidisciplinary Research*, **2024**, 6(3), 1-10.
[2] Yang, Z., Shen, J. A review: Metal and metal oxide nanoparticles for environmental applications. *Nanoscale*, **2025**.
[3] Abouri, M., Benzaouak, A., Zaaboul, F., Sifou, A., Dahhou, M., El Belghiti, M.A., Azzaoui, K., Hammouti, B., Rhazi, L., Sabbahi, R. Efficient catalytic reduction of organic pollutants using nanostructured CuO/TiO_2 catalysts: Synthesis, characterization, and reusability. *Inorganics*, **2024**, 12(11), 297.
[4] Mofid, H., Seyed Sadjadi, M., Hossaini Sadr, M., Banaei, A., Farhadyar, N. Green synthesis of zinc oxide nanoparticles using aloe vera plant for investigation of antibacterial properties. *Advances in Nanochemistry*, **2020**, 2(1), 32-35.
[5] Qu, B., Xiao, Z., Luo, Y. Sustainable nanotechnology for food preservation: Synthesis, mechanisms, and applications of zinc oxide nanoparticles. *Journal of Agriculture and Food Research*, **2025**, 19, 101743.
[6] Pani, S., Singh, S., Mohapatra, B. Synthesis and characterization of MnO nano-particles using thermal plasma technique. *Transactions of the Indian Institute of Metals*, **2019**, 72(1), 65-71.
[7] Premkumar, H., Perumal, R. Synthesis of ternary ZnO/CuO/MnO nanocomposite with crystalline and optical properties. *Optical Materials*, **2024**, 149, 114964.
[8] Raha, S., Ahmaruzzaman, M. Zno nanostructured materials and their potential applications: Progress, challenges and perspectives. *Nanoscale Advances*, **2022**, 4(8), 1868-1925.
[9] Haiouani, K., Hegazy, S., Alsaeedi, H., Bechelany, M., Barhoum, A. Green synthesis of hexagonal-like zno nanoparticles modified with phytochemicals of clove (syzygium aromaticum) and thymus capitatus extracts: Enhanced antibacterial, antifungal, and antioxidant activities. *Materials*, **2024**, 17(17), 4340.
[10] Chen, J., Zhou, Y., Islam, M.S., Cheng, X., Brown, S.A., Han, Z., Rider, A.N., Wang, C.H. Carbon fiber reinforced Zn–MnO_2 structural composite batteries. *Composites Science and Technology*, **2021**, 209, 108787.
[11] Khudhir, I.A., Essa, A. Preparation and characterization of polypyrrole/carbon nanotube composites using Zno, MgO and MnO. *Journal of Physics: Conference Series*, **2025**, 2974(1), 012029.
[12] EL-Moslamy, S.H., Rezk, A.H., Elkady, M., Shokry Hassan, H. Semi-Industrial Bio-Fabrication of ZnO/MnO_2 nanocomposite using endophytic streptomyces coelicolor: Characterization, statistical design, exponential pulse fed-batch fermentation, and its antimicrobial application. *Arabian Journal for Science and Engineering*, **2024**, 49(7), 9067-9088.
[13] Selim, S., Abdelghany, T.M., Almuhayawi, M.S., Nagshabandi, M.K., Tarabulsi, M.K., Elamir, M.Y.M., Alharbi, A.A., Al Jaouni, S.K. Biosynthesis and activity of Zn-MnO nanocomposite in vitro with molecular docking studies against multidrug resistance bacteria and inflammatory activators. *Scientific Reports*, **2025**, 15(1), 2032.
[14] Mahesh, B. A comprehensive review on current trends in greener and sustainable synthesis of ferrite nanoparticles and their promising applications. *Results in Engineering*, **2024**, 21, 101702.
[15] Hussein, B.A., Tsegaye, A.A., Shifera, G., Taddesse, A.M. A Sensitive Non-Enzymatic Electrochemical Glucose Sensor Based on a ZnO/Co 3 O 4 /Reduced Graphene Oxide Nanocomposite. *Sensors & Diagnostics*, **2023**, 2(2), 347-360.
[16] Hadžić, B., Romčević, N., Romčević, M., Kuryliszyn-Kudelska, I., Dobrowolski, W., Wróbel, R., Narkiewicz, U., Sibera, D. Raman study of surface optical phonons in ZnO (Mn) nanoparticles. *Journal of Alloys and Compounds*, **2014**, 585, 214-219.
[17] Hutera, B., Kmita, A., Olejnik, E., Tokarski, T. Synthesis of ZnO nanoparticles by thermal decomposition of basic zinc carbonate. *Archives of Metallurgy and Materials*, **2013**, 58.
[18] Kachallaa, M.R., Abdullahia, A., Yelwa, J.M., Aliyua, M.S. Green synthesis, characterization of manganese oxide nanoparticles using Ziziphus abyssinica plant extract and their antimicrobial efficacy. *Nanoscience and Nanotechnology: An Indian Journal*, **2022**, 16(6), 171.
[19] Zak, A.K., Abrishami, M.E., Majid, W.A., Yousefi, R., Hosseini, S. Effects of annealing temperature on some structural and optical properties of ZnO nanoparticles prepared by a modified sol–gel combustion method. *Ceramics International*, **2011**, 37(1), 393-398.
[20] Souri, M., Hoseinpour, V., Shakeri, A., Ghaemi, N. Optimisation of green synthesis of mno nanoparticles via utilising response surface methodology. *IET Nanobiotechnology*, **2018**, 12(6), 822-827.
[21] Shah, S.N., Ali, S.I., Ali, S.R., Naeem, M., Bibi, Y., Ali, S.R., Raza, S.M., Khan, Y., Sherwani, S.K. Synthesis and characterization of zinc oxide nanoparticles for antibacterial applications. *Journal of Basic & Applied Sciences*, **2016**, 12, 205-210.

[22] Saod, W.M., Hamid, L.L., Alaallah, N.J., Ramizy, A. Biosynthesis and antibacterial activity of manganese oxide nanoparticles prepared by green tea extract. *Biotechnology Reports*, **2022**, 34, e00729.
[23] Karam, S.T., Abdulrahman, A.F. Green synthesis and characterization of ZnO nanoparticles by using thyme plant leaf extract. *Photonics*, **2022**, 9(8), 594.
[24] Abdelhakim, H.K., El-Sayed, E.R., Rashidi, F.B. Biosynthesis of zinc oxide nanoparticles with antimicrobial, anticancer, antioxidant and photocatalytic activities by the endophytic Alternaria tenuissima. *Journal of Applied Microbiology*, **2020**, 128(6), 1634–1646.
[25] Ekennia, A., Uduagwu, D., Olowu, O., Nwanji, O., Oje, O., Daniel, B., Mgbii, S., Emma-Uba, C. Biosynthesis of zinc oxide nanoparticles using leaf extracts of alchornea laxiflora and its tyrosinase inhibition and catalytic studies. *Micron*, **2021**, 141, 102964.
[26] Peng, H., Ndione, P.F., Ginley, D.S., Zakutayev, A., Lany, S. Design of semiconducting tetrahedral $Mn_{1-x}Zn_xO$ alloys and their application to solar water splitting. *Physical Review X*, **2015**, 5(2), 021016.
[27] Abdelghani, G.M., Ahmed, A.B., Al-Zubaidi, A.B. Synthesis, characterization, and the influence of energy of irradiation on optical properties of zno nanostructures. *Scientific Reports*, **2022**, 12(1), 20016.
[28] Abdullah, O.G., Aziz, S.B., Omer, K.M., Salih, Y.M. Reducing the optical band gap of polyvinyl alcohol (pva) based nanocomposite. *Journal of Materials Science: Materials in Electronics*, **2015**, 26(7), 5303-5309.
[29] Jeevarathinam, M., Asharani, I. Synthesis of CuO, ZnO nanoparticles, and CuO-ZnO nanocomposite for enhanced photocatalytic degradation of rhodamine b: A comparative study. *Scientific Reports*, **2024**, 14(1), 9718.
[30] Marsalek, R. Particle size and zeta potential of ZnO. *APCBEE Procedia*, **2014**, 9, 13-17.
[31] Yang, C. Measuring zeta potential, methods. *Encyclopedia of Microfluidics and Nanofluidics*, **2015**, 1727-1737.
[32] Karvekar, O.S., Sarvalkar, P.D., Vadanagekar, A.S., Singhan, R.D., Jadhav, S.M., Nimbalkar, M.S., Prasad, N.R. Biogenic synthesis of silver anchored ZnO nanorods as nano catalyst for organic transformation reactions and dye degradation. *Applied Nanoscience*, **2022**, 12(7), 2207-2226.
[33] Faisal, S., Jan, H., Shah, S.A., Shah, S., Khan, A., Akbar, M.T., Rizwan, M., Jan, F., Wajidullah, Akhtar, N. Green synthesis of zinc oxide (zno) nanoparticles using aqueous fruit extracts of myristica fragrans: Their characterizations and biological and environmental applications. *ACS Omega*, **2021**, 6(14), 9709-9722.
[34] Nayan, M.B., Jagadish, K., Abhilash, M.R., Namratha, K., Srikantaswamy, S. Comparative study on the effects of surface area, conduction band and valence band positions on the photocatalytic activity of zno-m x o y heterostructures. *Journal of Water Resource and Protection*, **2019**, 11(03), 357.
[35] Worku, A.K., Ayele, D.W., Habtu, N.G. Influence of nickel doping on MnO_2 nanoflowers as electrocatalyst for oxygen reduction reaction. *SN Applied Sciences*, **2021**, 3(9), 764.
[36] Ahmed, F., Kumar, S., Arshi, N., Anwar, M., Su-Yeon, L., Kil, G.-S., Park, D.-W., Koo, B.H., Lee, C.G. Preparation and characterizations of polyaniline (pani)/ZnO nanocomposites film using solution casting method. *Thin Solid Films*, **2011**, 519(23), 8375-8378.
[37] Thi, T.U.D., Nguyen, T.T., Thi, Y.D., Thi, K.H.T., Phan, B.T., Pham, K.N. Green synthesis of zno nanoparticles using orange fruit peel extract for antibacterial activities. *RSC Advances*, **2020**, 10(40), 23899-23907.
[38] Li, L., Lu, Y., Chen, Y., Bian, J., Wang, L., Li, L. Antibacterial chitosan-gelatin microcapsules modified with green-synthesized silver nanoparticles for food packaging. *Journal of Renewable Materials*, **2023**, 11(1).
[39] Alqazaaly, S.M., Yaaqoob, L.A. Assessment of the antibacterial efficacy of nickel/manganese nanoparticles against Staphylococcus *aureus*. *BIO Web of Conferences*, **2025**, 173, 02022.
[40] Ajitha, B., Reddy, Y.A.K., Shameer, S., Rajesh, K., Suneetha, Y., Reddy, P.S. Lantana camara leaf extract mediated silver nanoparticles: Antibacterial, green catalyst. *Journal of Photochemistry and Photobiology B: Biology*, **2015**, 149, 84-92.
[41] Islam, M.F., Miah, M.A.S., Huq, A.O., Saha, A.K., Mou, Z.J., Mondol, M.M.H., Bhuiyan, M.N.I. Green synthesis of zinc oxide nano particles using allium cepa l. Waste peel extracts and its antioxidant and antibacterial activities. *Heliyon*, **2024**, 10(3).
[42] Hezam, A., Namratha, K., Drmosh, Q., Yamani, Z., Byrappa, K. Synthesis of Heterostructured Bi2O3–CeO_2–ZnO Photocatalyst with Enhanced Sunlight Photocatalytic Activity. *Ceramics International*, **2017**, 43(6), 5292-5301.
[43] Zolfaghari, M. Propose for raman mode position for MN-doped ZnO nanoparticles. *Physica B: Condensed Matter*, **2019**, 555, 1-8.
[44] Kanmani, S., Ramachandran, K., Umapathy, S. Eosin yellowish dye-sensitized ZnO nanostructure-based solar cells employing solid PEO redox couple electrolyte. *International Journal of Photoenergy*, **2012**, 2012(1), 267824.
[45] Cao, Q., Fu, M., Liu, G., Zhang, H., Yan, S., Chen, Y., Mei, L., Jiao, J. Local vibrational modes competitions in

MN-doped ZnO epitaxial films with tunable ferromagnetism. *Journal of Applied Physics*, **2014**, 115(24).
[46] Silambarasan, M., Saravanan, S., Soga, T. Raman and photoluminescence studies of ag and fe-doped zno nanoparticles. *International Journal of ChemTech Research*, **2015**, 7(3), 1644-1650.
[47] Dar, M., Narwaria, P., Barfa, S., Varshney, D. Structural and optical properties of combustion synthesized transition metal doped zn0. 94mn0. 06o nanoparticles. *AIP Conference Proceedings*, **2017**, 1832(1), 050052.
[48] Gatou, M.-A., Lagopati, N., Vagena, I.-A., Gazouli, M., Pavlatou, E.A. ZnO nanoparticles from different precursors and their photocatalytic potential for biomedical use. *Nanomaterials*, **2022**, 13(1), 122.
[49] Fischer, D., Zagorac, D., Schön, J.C. The presence of superoxide ions and related dioxygen species in zinc oxide—a structural characterization by in situ raman spectroscopy. *Journal of Raman Spectroscopy*, **2022**, 53(12), 2137-2146.
[50] Dieng, M., Ngom, B., Tall, P., Maaza, M. Biosynthesis of Zn5 (CO3) 2 (Oh) 6 from arachis hypogaea shell (peanut shell) and its conversion to zno nanoparticles. *American Journal of Nanomaterials*, **2019**, 7(1), 1.
[51] Zhao, L., Gong, K., Wang, Y., Kong, S. Rapid and environment-friendly preparation of silver nanoparticles and their inhibition against phytopathogenic fungi. *Micro & Nano Letters*, **2021**, 16(3), 213-220.
[52] Bishoyi, A.K., Sahoo, C.R., Sahoo, A.P., Padhy, R.N. Bio-synthesis of silver nanoparticles with the brackish water blue-green alga oscillatoria princeps and antibacterial assessment. *Applied Nanoscience*, **2021**, 11(2), 389-398.
[53] Goutam, S.P., Yadav, A.K., Das, A.J. Coriander extract mediated green synthesis of zinc oxide nanoparticles and their structural, optical and antibacterial properties. *Journal of Nanoscience and Technology*, **2017**, 249-252.
[54] Kora, A.J., Rastogi, L. Enhancement of antibacterial activity of capped silver nanoparticles in combination with antibiotics, on model gram-negative and gram-positive bacteria. *Bioinorganic Chemistry and Applications*, **2013**, 2013(1), 871097.
[55] Mahamuni, P.P., Patil, P.M., Dhanavade, M.J., Badiger, M.V., Shadija, P.G., Lokhande, A.C., Bohara, R.A. Synthesis and characterization of zinc oxide nanoparticles by using polyol chemistry for their antimicrobial and antibiofilm activity. *Biochemistry and Biophysics Reports*, **2019**, 17, 71-80.
[56] Kong, J., Zhang, J., Shen, M., Zhang, S., Shen, P., Ren, C. Preparation of manganese (ii) oxide doped zinc oxide nanocomposites with improved antibacterial activity via ros. *Chemical Physics Letters*, **2022**, 806, 140053.
[57] Faraji, N., Hajimahdi, Z. Synthesis, characterisation, and antimicrobial activity of zno-based nanocomposites. *Micro & Nano Letters*, **2018**, 13(12), 1667-1671.

HOW TO CITE THIS MANUSCRIPT
C. Maalegoundla, N. Pusapati, L.S. Boddu, P.K. Naini, S. T. Zn-MnO Nanocomposites Derived from *Cocos nucifera*: A Multi-Analytical Characterisation and Antimicrobial Study. *Asian Journal of Green Chemistry*, 10 (4) 2026, 694-717.
DOI: https://doi.org/10.48309/ajgc.2026.554745.1852
URL: https://www.ajgreenchem.com/article_238820.html